COBEM 2023 27TH INTERNATIONAL CONGRESS OF MECHANICAL ENGENEERING

ABCM Brazilian Society of Mechanical Sciences and Engineering
27th ABCM International Congress of Mechanical Engineering
December 04-08, 2023, Florianópolis-SC, Brazil

COB-2023-2064
DIGITAL IMAGE CORRELATION APPLIED TO INTERFACE TRACKING DURING FLOW BOILING IN MICROCHANNELS

Debora Carneiro Moreira
Jorge Nicolau dos Santos
Heat Transfer Research Group (HTRG), Department of Mechanical Engineering, São Carlos School of Engineering – University of São Paulo (EESC/USP)
dcmoreira@usp.br
jorgenic@sc.usp.br

Valter Salles do Nascimento Junior
INCT NAMITEC, Institute of Electrical and Compuuttional Engineering – State University of Campinas (FEEC/UNICAMP)
valtersallesjr@gmail.com

Gherhardt Ribatski
Heat Transfer Research Group (HTRG), Department of Mechanical Engineering, São Carlos School of Engineering – University of São Paulo (EESC/USP)
ribatski@sc.usp.br

Abstract. *The use of heat sinks based on flow boiling in microchannels has been widely investigated over the last decades, mainly due to the ability of dissipating high heat loads from restricted spaces with minimum temperature gradients throughout the devices. Despite these desirable characteristics for thermal management technologies, most investigations from the literature still rely on empirical observations and parametric studies, while fundamental aspects regarding the phenomena are yet to be understood. Recently, encouraging flow boiling heat transfer results were obtained with microstructured surfaces containing asymmetric Dual-V microchannels with an open and tapered manifold. The performance was attributed to the successful combination of strategies previously employed to enhance pool and flow boiling heat transfer, promoting bubble crossflow and inducing separate liquid and vapor pathways. High-speed images of the flow patterns during those experiments were associated with the operational conditions and parameters of interest, like pressure drop and heat transfer coefficient. However, it should be noted that these images can also reveal the locations of active nucleation sites, be used to estimate the single-phase length, the bubble departure diameters and frequencies, bubble trajectories, and the occurrence of instabilities and back-flow, for example. The main goal of this work is to process the acquired full-field high speed images in order to track the generated interfaces through the digital image correlation method and assess the displacements and velocities of the interfaces. The interface identification and displacement calculations were implemented using MATLAB scripts, and the evolution of flow patterns related to each condition was observed in full-field images, revealing the activation of nucleation sites at upstream portions of the channels and the establishment of liquid-vapor preferential paths. Finally, the image analysis was applied to image sequences obtained at various experimental conditions, and the observations were compared with heat transfer performances and calculated single-phase lengths, showing good agreement between theoretical and experimental results and supporting that the performance improvement is directly related to the generation of preferential liquid and vapor paths.*

Keywords: *Cross-correlation, DIC, Bubble, Two-phase flow, High-speed imaging.*

1. INTRODUCTION

The interest in high heat flux cooling technologies is continuously growing, since the development of high-power electronics and the miniaturization of components generate demands for heat dissipation that are already reaching the order of 10 MW/m^2 (Ding et al., 2020; Dwivedi et al. 2020). In addition, most of these devices require precise temperature management to guarantee their best performances and prevent catastrophic failure. During the last decades, investigations on microchannel flow boiling have shown its great potentials to overcome this challenge, with desirable features like relatively stable operating temperature allied to high heat transfer efficiency (Ribatski, 2013), but some challenges were faced in the development of these devices, such as severe instabilities, flow reversal, high pressure drop and premature critical heat flux (CHF) (Kandlikar, 2012). Thus, many works have focused on the proposition of diverse geometries and surface structuration to improve the performance of flow boiling in microchannel heat sinks (Benam et al., 2021). Recently, Moreira et al. (2022a, 2023) presented a design of copper microchannel heat sink based on Dual-V grooves

combined with an open tapered manifold previously proposed by Kandlikar et al. (2013), and reported remarkable performances with water (Moreira et al., 2022a) and R1336mzz(Z) (Moreira et al., 2023) as working fluids, achieving the dissipation of up to 728 kW/m^2 with HTC that reached 16.7 kW/m^{2}K and a pressure drop lower than 10 kPa with the refrigerant. The outstanding heat transfer performance with low pressure drop and stable flow was attributed to the organization of the flow into preferential liquid and vapor paths, which ensured continuous liquid supply and vapor removal to and from the surface, in a similar manner as was observed in previous works regarding pool boiling (Kandlikar, 2013; Jaikumar and Kandlikar, 2015, 2016). In addition, the occurrence of boiling inversion (Jaikumar and Kandlikar, 2017) during experiments with water was reported for the first time for flow boiling, and this phenomenon was also attributed to the separated liquid-vapor pathways induced by the surface geometry (Moreira et al., 2022a).

The relation between the thermal and hydraulic parameters to the flow morphology created by the interaction with the Dual-V microstructured surface was supported by the identification of crossflow movement of single bubbles observed with a high-speed camera, as described by Moreira et al. (2022b). However, the full-field flow patterns were only analyzed through a qualitative approach, in which the separation of vapor and liquid paths were visually identified (Moreira et al., 2022a). In this context, this work comprises a thorough analysis of the full-field high-speed images acquired during flow boiling experiments with R1336mzz(Z) in order to assess some quantitative parameters regarding the flow patterns. The Digital Image Correlation (DIC) technique was applied to each sequence of images to track the displacements of liquid-vapor interfaces, then the interface velocities were calculated along the heat sink, and it was possible to identify the most active nucleation regions. The influence of various parameters on the observed results was analyzed, like the image acquisition frequency, the length of the videos, the dimensions of interrogation areas and their distribution. After the best conditions for the analyses were defined, the technique was applied to distinct sequences of images and the results were evaluated according to the experimental conditions, like the variation of heat and mass flux. Based on the observed results, the DIC technique can be applied to quantitatively analyze images from flow boiling experiments, with successful identification of increasing nucleation activity at the upstream portion of the heat sink as the heat flux increased and mass flux decreased. Nevertheless, it should be noted that the increasingly chaotic behavior on the downstream portion of the heat sink with the flow pattern turning into a churn flow may lead to wrong values of flow velocities. Finally, the importance of proper illumination should not be neglected, and it is expected that better results can be achieved by employing a diffuse and stronger illumination setup.

2. MATERIALS AND METHODS

The experimental campaign from this work is part of a broad investigation performed by Moreira et al. (2023), such that the configuration of the test section, experimental apparatus and test conditions are briefly described in this section, while further details can be found in our previous work (Moreira et. al, 2023). The test section used in this work consisted of a copper chip with microstructured surface designed to interact with nucleating bubbles and direct them in a certain way to create preferential liquid and vapor paths, similarly to what was proposed by Kandlikar (2013) for pool boiling. Thus, the concept of the employed surface was based on pairs of asymmetric V-shaped microchannels, called Dual-V grooves, which were machined in copper chips along the 10 mm flow length. The expected trajectory of nucleating bubbles is shown schematically for an asymmetric Dual V-groove with one side normal to the base as seen in Fig. 1, reprinted from (Moreira et al., 2022), and heat was applied to the flow through the 10 mm x 10 mm footprint area. The copper chips were combined with a tapered manifold fabricated in polysulfone that defined the flow area and enabled flow visualization, using a similar geometry that presented the best performance in the work of Kalani and Kandlikar (2015a,b), with a 6% taper, meaning that the gap height above the channels top increased by 600 μm, from 180 to 780 μm along the 10 mm length of the channels. Images from experiments conducted with a sample containing five Dual-V channels with internal angles equal to 30° and 400 μm high walls above the reference surface were used in this work.

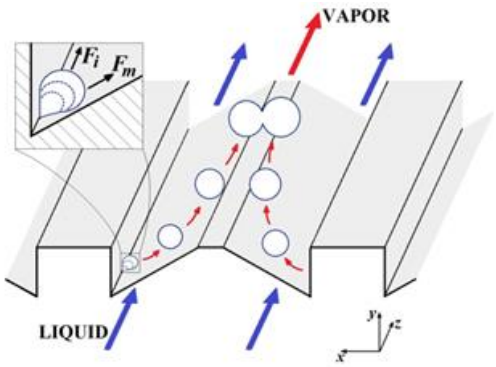

Figure 1. Expected trajectories of nucleating bubbles in the Dual-V groove microchannels. Reprinted from (Moreira et al., 2022).

Full-field flow images were acquired with a Phantom v2012 CMOS monochromatic ultrahigh-speed camera and a 105 mm Micro-Nikkor f/2.8 lens, set at 30000 fps and 1/40000 s^{-1} shutter speed, with a resolution of 304 pixels corresponding to the gap width and channel length of 10 mm. The illumination system was composed of a single 50 W LED reflector with a home-made soft box to create a homogeneous diffuse illumination. A mirror positioned at 45° reflected the image from the top of the heat sink to the camera, which was fixed to a tripod. Most of the videos were recorded for 0.5 s, but some sequences were recorded for up to 2.5 s, so the effect of longer acquisition times could also be evaluated. The high acquisition rate during the experiments enabled the analysis of the impact of different acquisition rates during the image processing, which was carried out by analyzing one of every "*k*" images for an effective rate equal to "*30000/k*" fps. Moreover, varying size of parts in which each image was divided as well as their distribution were analyzed in order to extract the maximum information from the available images. The image processing procedure is illustrated in Fig. 2 and explained in more detail in the following sections.

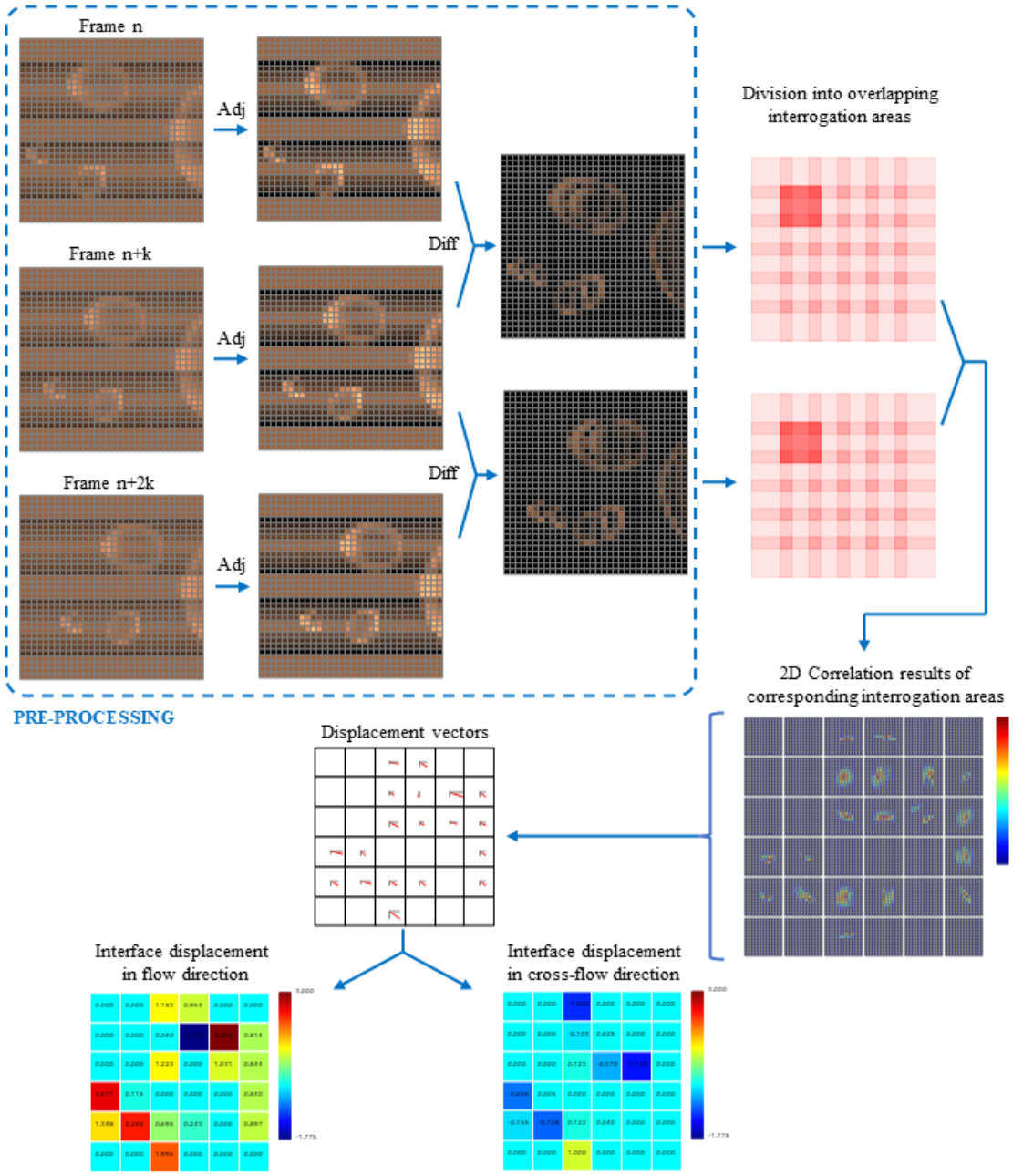

Figure 2. Graphical illustration of the procedure to identify the interfacial displacements from a sequence of images.

2.1 Image pre-processing

Each sequence of images was submitted to a pre-processing procedure in order to remove the background and enhance the contrast of the interfaces. Then, the interface displacement of the resulting images was tracked. For each

monochromatic image with the luminance associated with each pixel varying from 0.0 to 1.0, with 1.0 being a theoretical perfect reflector of 100% reference white, this monochromatic image $\boldsymbol{A}$ with dimensions N x M can be written as a matrix:

$$\boldsymbol{A} = \left\{ p_{A_{i,j}} | i = 1,2,\dots,M; j = 1,2,\dots,N; 0 \le p_{A_{i,j}} \le 1 \right\} \tag{1}$$

The function *Adj* applied to $\boldsymbol{A}$ stretches the luminance range of $\boldsymbol{A}$, as seen:

$$Adj(\boldsymbol{A}) = \left\{ p_{i,j} = \frac{p_{A_{i,j}} - \min(A)}{\max(A) - \min(A)} \middle| i = 1,2,\dots,M; j = 1,2,\dots,N; 0 \le p_{i,j} \le 1 \right\}, \tag{2}$$

then the function *Diff* is applied to two consecutive frames with the same dimensions, identified as $\boldsymbol{A}$ and $\boldsymbol{B}$, calculating the absolute luminance difference of each pixel, defined as:

$$Diff(\boldsymbol{A}, \boldsymbol{B}) = \left\{ p_{i,j} = \left| p_{\boldsymbol{A}_{i,j}} - p_{\boldsymbol{B}_{i,j}} \right| \middle| i = 1,2,\dots,M; j = 1,2,\dots,N; 0 \le p_{i,j} \le 1 \right\}. \tag{3}$$

This operation removes the common background from the original frames and highlights the interfacial displacements in the resulting matrix.

The image preprocessing algorithm was developed based on these functions, and for three consecutive frames $\boldsymbol{A}$, $\boldsymbol{B}$ and $\boldsymbol{C}$, it has the following steps:

$$\begin{aligned} &\boldsymbol{A}_{Adj} \leftarrow Adj(\boldsymbol{A}) \\ &\boldsymbol{B}_{Adj} \leftarrow Adj(\boldsymbol{B}) \\ &\boldsymbol{C}_{Adj} \leftarrow Adj(\boldsymbol{C}) \\ &\boldsymbol{AB} \leftarrow Diff(\boldsymbol{A}_{Adj}, \boldsymbol{B}_{Adj}) \\ &\boldsymbol{BC} \leftarrow Diff(\boldsymbol{B}_{Adj}, \boldsymbol{C}_{Adj}) \end{aligned} \tag{4}$$

Once the differences $\boldsymbol{AB}$ and $\boldsymbol{BC}$ are calculated, the interfacial displacements can be assessed through an in-plane cross-correlation function applied to small portions of the image defined as *interrogation areas*, as described in the next section.

2.2 Interfacial displacements calculation

The pre-processing was applied to the whole set of images, so the temporal displacements between portions of each frame difference were assessed, then an average displacement was calculated for each portion of the full-field image. The interfacial displacements were obtained by the cross-correlation of interrogation areas at the same position of two consecutive pre-processed images. Thus, for a preprocessed image $\boldsymbol{A}$ with resolution N x M pixels, an interrogation area IA_{mn} is defined as:

$$IA_{mn} = \left\{ p_{ij} \middle| i = r, r+1, \dots, R_{IA}; j = c, c+1, \dots, C_{IA} \right\} \tag{5}$$

Where r and c are the respective column and row from the full-field image $\boldsymbol{A}$, and the dimensions of the interrogation area should be equal to or smaller than those of the image A:

$$R_{IA} \le M \quad \text{and} \quad C_{IA} \le N \tag{6}$$

The interrogation areas were allowed to overlap, in order to increase the number of displacement vectors and minimize the contour error without losing information that could reduce the feasibility of the cross-correlation process. The overlapping was set by the user in two parameters: OL_r and OL_c, respectively for rows and columns. The bubble interfaces displacement vectors are obtained by the cross-correlation of the same interrogation area of two sequential preprocessed images $\boldsymbol{AB}$ and $\boldsymbol{BC}$, first applying a Hanning window function in the interrogation area to minimize the contour discontinuity error of the Fast Fourier Transform, and the algorithm for this process is:

$$\begin{aligned} &FOR \text{ each } IA \text{ centered in column } x \text{ and row } y \\ &\quad \boldsymbol{D} \leftarrow \text{Hanning}\left(IA(\boldsymbol{AB})\right) \circledast \text{Hanning}\left(IA(\boldsymbol{BC})\right) \\ &\quad IF \text{ there is a maximum value element of } \boldsymbol{D} \\ &\qquad (u, v) \leftarrow indexes\ (i, j)\ of\ the\ maximum\ value\ element\ d_{i,j}\ of\ \boldsymbol{D} \\ &\qquad \Delta u \leftarrow [\log(du, v-1) - \log(du, v+1)] \\ &\qquad\qquad / [2\ (\log(du, v-1) - 2\ \log(du, v) + \log(du, v+1))] \end{aligned} \tag{7}$$

$$\Delta v \leftarrow [\log(u-1,dv) - \log(u+1,dv)] \\ /[2\ (\log(u-1,dv) - 2\ \log(u,dv) + \log(u+1,dv))]$$
$$(u,v) \leftarrow (u+\Delta u, v+\Delta v)$$
$$ELSE$$
$$(u,v) \leftarrow (0,0)$$
$$END\ IF$$
$$END\ FOR$$

The calculation of Δu and Δv allows an improvement to the displacement assessment by the inclusion of a possible subpixel displacement based on a two-dimensional Gaussian regression (Willert and Gharib, 1991). The resulting *(u,v)* vector are the bubble interfaces displacement components of the interrogation area centered in column *x* and row *y* in pixels.

In order to obtain the displacements in mm, it is necessary to convert pixels to mm, which can be done using the equations:

$$X = \left(\frac{L_c}{N}\right)u \qquad \text{and} \qquad Y = \left(\frac{W_g}{M}\right)v, \tag{8}$$

where *X* and *Y* are the displacements in mm of the interrogation area, L_c is the length of the channels and W_g is the gap width, both measuring 10 mm. The velocity components *U* and *V* can be calculated based on the displacements divided by the time step between two consecutive frames, Δt:

$$U = \frac{X}{\Delta t} \qquad \text{and} \qquad V = \frac{Y}{\Delta t} \tag{9}$$

with

$$\Delta t = \frac{1}{fps} \tag{10}$$

and *fps* is the image acquisition rate. These calculations were carried out for average *u* and *v* displacements of the entire video corresponding to the evaluated experimental condition.

3. RESULTS AND DISCUSSION

Results obtained through the application of the Digital Image Correlation method to sets of high-speed images are presented in this section. First, the evaluation of the parameters related to the image processing are presented, so some optimum conditions could be defined prior to the evaluation of images obtained for varying experimental conditions. Then the analysis for distinct experimental conditions is presented, and the results from this investigation were compared to the thermal-hydraulic performances reported by Moreira et al. (2023).

3.1 Varying image analysis parameters

The first parameters that needed to be defined in order to proceed with the DIC method were the size and quantity of interrogation areas in the region of interest. It is worth highlighting that poor results can be obtained if the interrogation areas are too small or too large, since small regions with only few points might correlate with anything in the deformed interrogation area, while large regions result in lower resolution of the displacement fields and may present significant relative deformations over the whole area and hinder the correlation with the original image. Figure 3 shows the displacement fields observed for the same sequence of images obtained in an experiment with inlet mass flux of 600 kg/m^{2}s for a heat flux of 37.7 W/cm^2 that were processed with varying sized interrogation areas.

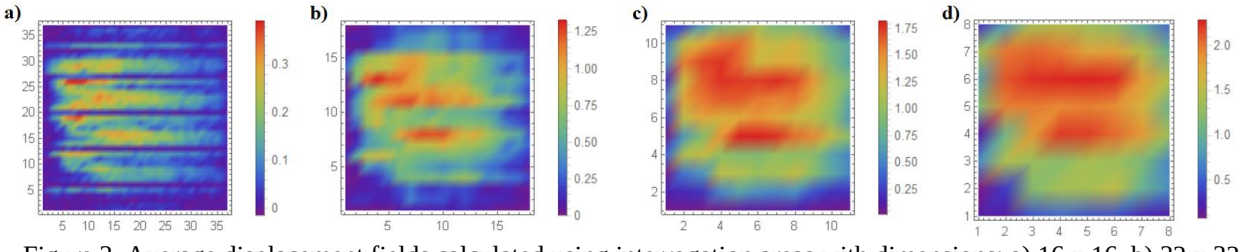

Figure 3. Average displacement fields calculated using interrogation areas with dimensions: a) 16 x 16, b) 32 x 32, c) 48 x 48 and d) 64 x 64 with horizontal and vertical overlaps equivalent to half the size of the interrogation area.

According to Fig. 3, the smallest interrogation areas yielded better results, where it is possible to observe larger interfacial displacements related to the channel regions, as expected and visually identified in our previous work. As already mentioned, the routine employed in this work enabled the overlapping of interrogation areas, therefore the number of elements was not limited by their size ratio to the full resolution and the displacement fields could be refined using larger interrogation areas. Figure 4 presents the evaluation of average interface displacements in the flow direction for the same sequence of images with elements containing 32 x 32 pixels for varying vertical and horizontal overlapping.

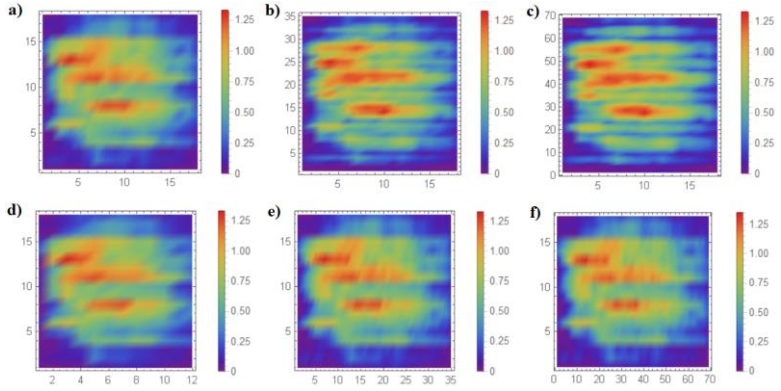

Figure 4. Average displacement fields observed in an experiment with inlet mass flux of 600 kg/m^{2}s for a heat flux of 37.7 W/cm^2. The horizontal and vertical overlappings of the interrogation areas were: a) OL_r: 16 and OL_c: 16, b) OL_r: 24 and OL_c: 16, c) OL_r: 28 and OL_c: 16, d) OL_r: 16 and OL_c: 8, e) OL_r: 16 and OL_c: 24 and f) OL_r: 16 and OL_c: 28.

It can be noticed that the row overlapping makes a significant difference when it is increased from 16 to 24 pixels, and the channel structures are revealed in higher definition as we have more interrogation areas, and the visualization of the displacement fields is refined. In contrast, the column overlapping does not present a significant improvement for the selected size of interrogation area, which can be attributed to the continuity of the channels in this direction, such that further refinement of the domain could not provide additional information. In fact, even for a column overlapping of 8 pixels the obtained results have not differed much from the ones with larger overlapping. The analyses that were carried out from this point were all based in square interrogation areas with 32 x 32 pixels and vertical and horizontal overlappings of 16 pixels.

The acquisition rate was the next parameter that was evaluated, which was set to 30000 fps during the experiments, but its variation during post-processing was achieved by adding steps to the image loading that changed the effective acquisition rate based on the sequence of images that were analyzed. Since the acquisition time remained the same, the number of images that were analyzed at lower rates were proportionally reduced. Figure 5 shows the displacement fields observed for the sequence of images obtained in an experiment with inlet mass flux of 600 kg/m^{2}s for a heat flux of 41.5 W/cm^2, and the effective acquisition rate varied from 300 to 30000 fps.

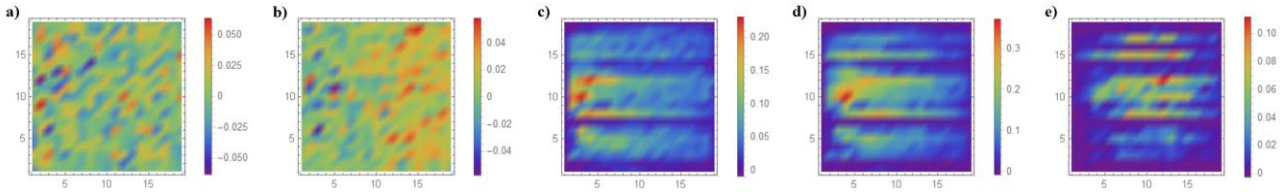

Figure 5. Average displacement fields calculated for acquisition rates od: a) 300 fps, b) 600 fps, c) 3000 fps, d) 6000 fps and e) 30000 fps.

Based on the characteristic times of bubble nucleation, growth and detachment, it was already expected that an acquisition rate of the order of 1 kHz was enough to capture the boiling phenomena, and the results displayed in Fig. 5 are in agreement with such expectations. However, other interesting observations can be drawn based on these results, as the displacement fields calculated with acquisition rates of 300 and 600 fps were null, and the highest acquisition rate pointed to a region of larger displacements that is different from what was observed for 3000 and 6000 fps, and the inner channel regions are also showing higher displacements for the highest rate. Thus, it can be speculated that at the highest acquisition rate we are able to capture more information on the beginning of the bubble cycle, while they are growing inside the channels at a more intense activity downstream the channels, while at 3000 and 6000 fps we see more of the bubble interfaces that are flowing in the open manifold region, mainly carried by the flow. However, such hypothesis requires a thorough and careful investigation.

The last parameter in image processing that was analyzed was the video length, or acquisition time. One should have in mind that reductions in acquisition rate and time have significant impact on the processing time and storage

requirements, which may be even more relevant, especially for high-quality images. Hence, the impact of varying the acquisition time was evaluated for the same image sequence that was analyzed in Fig. 5, using an effective acquisition rate of 6000 fps, while the acquisition time varied from 0.1 s to 1.5 s, which was carried out simply by selecting the first images of that sequence that corresponded to the desired video length, and the obtained results are seen in Fig. 6.

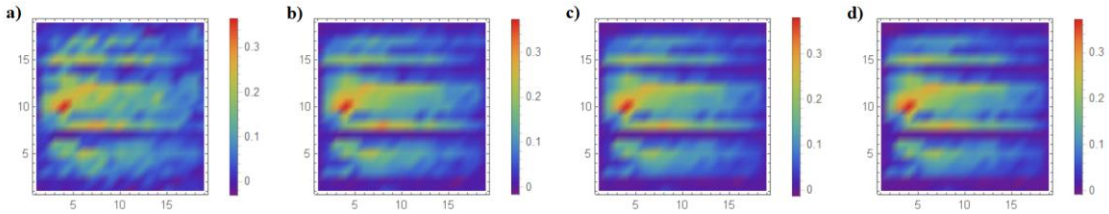

Figure 6. Average displacement fields observed in an experiment with inlet mass flux of 600 kg/m^{2}s for a heat flux of 41.5 W/cm^2. The considered acquisition times were: a) 0.1 s, b) 0.5 s, c) 1.0 s and d) 1.5 s.

According to Fig. 6, the variation of acquisition time for the selected conditions had negligible effect in the average displacement fields that were calculated, especially from 0.5 s to higher times. Based on the results that were exposed in this section, sequences of images acquired for various experimental conditions were evaluated using fixed processing parameters. Interrogation areas with dimensions of 32 x 32 pixels were selected, and the overlapping was set to 24 pixels. The effective acquisition rate was set to 6000 fps, and the acquisition time to 0.5 s. Results for varying experimental parameters are presented and discussed in the next section.

3.2 Varying experimental conditions

Moreira et al. (2023) conducted experiments for four distinct values of inlet mass flux varying from 400 to 1000 kg/m^{2}s, and for each mass flux the heat flux increased from single-phase conditions up to the critical heat flux with the sample containing five pairs of Dual-V microchannels. It was pointed out that the activation of nucleation sites closer to the upstream portion of the channels was observed as the heat flux was increased, especially at low heat fluxes, and that for higher heat fluxes the nucleation activity in the channels intensified and resulted in an organization of the flow into preferential liquid and vapor paths. Figure 7 presents the evaluation of some image sequences from the experiments conducted by Moreira et al. (2023) for an inlet mass flux of 600 kg/m^{2}s with the methodology presented in this work.

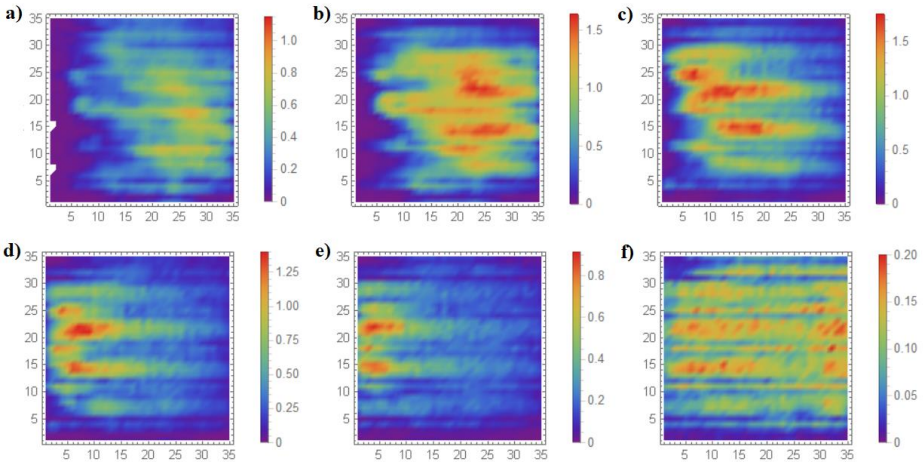

Figure 7. Average displacement fields observed in an experiment conducted with inlet mass flux of 600 kg/m^{2}s for heat fluxes of: a) 16.6 W/cm^2, b) 24.9 W/cm^2, c) 33.1 W/cm^2, d) 41.5 W/cm^2, e) 45.6 W/cm^2 and f) 49.8 W/cm^2.

It is possible to observe that the interface displacements are stronger at the downstream portion of the heat sink for lower heat fluxes, but the region with larger displacements moves towards the upstream portion of the heat sink as the heat fluxes increases. However, for the highest heat flux, at CHF conditions, it is possible to see that the calculated displacements significantly reduce and are more equally distributed over the heat sink, which occurs due to the lack of interfaces to be identified, which would reduce the reliability of the actual values of displacements and velocities at this condition. In addition, it should be noted that the maximum average displacements did not change much as the heat flux increased from 24.9 to 41.5 W/cm^2. In contrast to what is observed when the heat flux is increased, increases in mass flux push the largest displacements towards the downstream region of the heat sinks as the single-phase length is increased, as seen in Fig. 8. The present discussion clearly supports what was previously discussed by Moreira et al. (2023).

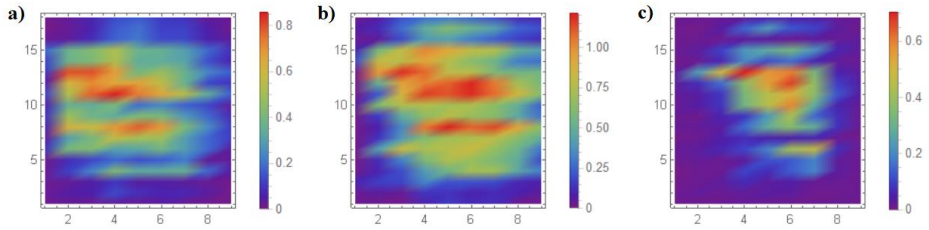

Figure 8. Average displacement fields observed in an experiment conducted with inlet mass flux of 600 kg/m^{2}s for heat flux of 32.5 W/cm^2 and inlet mass flux equal to: a) 400 kg/m^{2}s, b) 600 kg/m^{2}s and c) 1000 kg/m^{2}s.

4. CONCLUSIONS

The present work has successfully applied the DIC technique to identify liquid-vapor interfaces from images acquired during flow boiling experiments from our previous work. The rise in nucleation activity at the upstream portion of the heat sink for an increasing heat flux and reduction in mass flux could be observed through the location of the regions with larger average displacements. Nevertheless, it should be noted that the increasing chaotic behavior on the downstream portion of the heat sink with the flow pattern turning from bubbles with sharp contours into a churn flow may lead to wrong values of displacements and velocities. Further investigation must be carried out in order to evaluate the extension of application of the current technique and to compare theoretical velocities to interfacial velocities that can be calculated using the current technique.

5. ACKNOWLEDGEMENTS

The authors would like to acknowledge the financial support provided by FAPESP through the grants #2015/24834-3, #2016/09509-1, #2017/12576-5, and #2018/23538-0. The technical support provided by Rick Wurzer and Craig Arnold from the ME Department at RIT in the fabrication of the microstructured copper chips and manifolds is also recognized and deeply appreciated.

6. REFERENCES

Benam, B. P., Sadaghiani, A. K., Yağcı, V., Parlak, M., Sefiane, K. and Koşar, A., 2021. Review on high heat flux flow boiling of refrigerants and water for electronics cooling. *International Journal of Heat and Mass Transfer*, 180, 121787.

Ding, B., Zhang, Z. H., Gong, L., Xu, M. H. and Huang, Z. Q., 2020. A novel thermal management scheme for 3D-IC chips with multi-cores and high power density. *Applied Thermal Engineering*, 168, 114832.

Dwivedi, P., Sudhakar, K., Soni, A., Solomin, E. and Kirpichnikova, I., 2020. Advanced cooling techniques of PV modules: A state of art. *Case Studies in Thermal Engineering*, 21, 100674.

Jaikumar, A. and Kandlikar, S. G., 2015. Enhanced pool boiling heat transfer mechanisms for selectively sintered open microchannels. *International Journal of Heat and Mass Transfer* 88, 652-661.

Jaikumar, A. and Kandlikar, S. G., 2016. Ultra-high pool boiling performances and effect of channel width with selectively coated open microchannels. *International Journal of Heat and Mass Transfer* 95, 795-805.

Jaikumar, A. and Kandlikar, S. G., 2017. Pool boiling inversion through bubble induced macroconvection. *Applied Physics Letters* 110, 094107.

Kalani, A., and Kandlikar, S. G., 2015a. Flow patterns and heat transfer mechanisms during flow boiling over open microchannels in tapered manifold (OMM). *International Journal of Heat and Mass Transfer*, Vol. 89, pp. 494-504.

Kalani, A. and Kandlikar, S.G., 2015b. Effect of taper on pressure recovery during flow boiling in open microchannels with manifold using homogeneous flow model. *International Journal of Heat and Mass Transfer*, Vol. 83, pp. 109-117.

Kandlikar, S. G., 2012. History, advances, and challenges in liquid flow and flow boiling heat transfer in microchannels: a critical review. *Journal of heat transfer*, 134(3).

Kandlikar, S. G., 2013. Controlling bubble motion over heated surface through evaporation momentum force to enhance pool boiling heat transfer. *Applied Physics Letters*, Vol. 102(5), pp. 051611.

Kandlikar, S. G., Widger, T., Kalani, A. and Mejia, V., 2013. Enhanced flow boiling over open microchannels with uniform and tapered gap manifolds. *Journal of Heat Transfer*, 135(6).

Moreira, D. C., do Nascimento Jr., V. S., Ribatski, G., Kandlikar, S. G., 2022. Combining liquid inertia and evaporation momentum forces to achieve flow boiling inversion and heat transfer performance enhancement, *International Journal of Heat and Mass Transfer*, 194, 123009.

Moreira, D. C., dos Santos, J. N., Nascimento Jr, V.S., Ribatski, G. and Kandlikar, S.G. 2022b. High-speed imging of flow boiling in asymmetric Dual-V microchnnels with tapered manifold. *In Proceedings of the 19th Brazilian Congress of Thermal Sciences and Engineering*. Virtual Conference, Brasil.

Moreira, D. C., do Nascimento Jr., V. S., Ribatski, G., Kandlikar, S. G., 2023. Flow boiling of R1336mzz(Z) in tapered microgaps with asymmetric dual-V microchannels, *Applied Thermal Engineering*, 228, 120440.
Ribatski, G., 2013. A critical overview on the recent literature concerning flow boiling and two-phase flows inside micro-scale channels. *Experimental Heat Transfer*, 26(2-3), 198-246.
Willert, C. E., and Gharib, M. (1991). Digital particle image velocimetry. *Experiments in fluids*, 10(4), 181-193.

7. RESPONSIBILITY NOTICE

The authors are the only ones responsible for the printed material included in this paper.